ADVANCED ENERGY MATERIALS
www.advenergymat.de

Chemical and Structural Degradation of Single Crystalline High-Nickel Cathode Materials During High-Voltage Holds

Kilian Vettori, Steffen Schröder, Lara Ahrens, Rebecca Wilhelm, Sascha Kremer, Janis K. Eckhardt, Torsten Brezesinski, Aleksandr Kondrakov, Joachim Mayer, Anja Henss,* and Jürgen Janek**

Enhancing the energy density of lithium-ion batteries (LIB) by increasing the nickel content in layered transition metal oxides is challenging due to accelerated degradation at high potentials. Here, degradation of single crystalline $LiNi_{0.83}Co_{0.11}Mn_{0.06}O_2$ (NCM831106) is investigated during prolonged, constant potential holds (U_{hold} = 4.5 V versus Li^+/Li), using transmission electron microscopy (TEM), secondary ion mass spectrometry, and X-ray photoelectron spectroscopy. Electrochemical impedance spectroscopy reveals a novel non-linear increase in charge transfer resistance of the cathode over time. The findings show that after initial thinning, the CEI exhibits notable stability in composition and structure during prolonged holds. In contrast, the growth of a cubic, rock salt-like surface reconstruction layer (SRL) at the NCM surface is continuous. TEM image processing provides detailed insights into the non-uniform spatial distribution of the SRL. Employing a resistor network model, it is proposed that this spatially inhomogeneous, resistive SRL and consequent local current constrictions explain the non-linear resistance increase. These findings contribute to the understanding of cathode degradation during long-term high-voltage operation, i.e., when LIBs are maintained in a highly charged state. These results highlight, that progressive SRL formation, rather than CEI changes, dictates the evolution of kinetic limitations for high-Ni NCM.

1. Introduction

The transition from combustion toward electric engines for automotive applications requires energy storage systems with high energy density and mass specific energies far above 200 Wh kg^{-1}.[1] After conquering the consumer electronics market the lithium-ion battery (LIB) has emerged as the state of the art solution also for electric vehicles (EV). One strategy to further increase the specific energy of typical LIBs consisting of a layered transition metal oxide such as $LiNi_aCo_bMn_cO_2$ (NCM), a liquid electrolyte and a graphite anode, is to increase the nickel content in the cathode active material (CAM). While these high-Ni CAMs deliver higher capacities, they suffer from enhanced degradation and ultimately less stability, due to larger volume changes during de/lithiation and higher surface reactivity.[2–4] This issue is particularly pronounced at high potentials exceeding 4.3 V versus Li^+/Li, corresponding to the charged or

K. Vettori, S. Kremer, J. Janek
Institute of Physical Chemistry
Justus Liebig-University Giessen
Heinrich-Buff-Ring 17, 35392 Giessen, Germany
E-mail: kilian.vettori@uni-giessen.de;
juergen.janek@phys.chemie.uni-giessen.de

K. Vettori, S. Schröder, S. Kremer, J. K. Eckhardt, A. Henss, J. Janek
Center for Materials Research (ZfM)
Justus Liebig-University Giessen
Heinrich-Buff-Ring 16, 35392 Giessen, Germany
E-mail: anja.henss@uni-giessen.de

The ORCID identification number(s) for the author(s) of this article can be found under https://doi.org/10.1002/aenm.202502148

DOI: 10.1002/aenm.202502148

S. Schröder, A. Henss
Institute of Experimental Physics I
Justus Liebig-University Giessen
Heinrich-Buff-Ring 16, 35392 Giessen, Germany

L. Ahrens
Central Facility for Electron Microscopy (GFE)
RWTH Aachen University
Ahornstr. 55, 52074 Aachen, Germany

L. Ahrens, J. Mayer
Ernst Ruska-Centre for Microscopy and Spectroscopy with Electrons (ER C)
Forschungszentrum Jülich GmbH
Wilhelm-Johnen-Straße, 52428 Jülich, Germany

R. Wilhelm
TUM School of Natural Sciences, Department of Chemistry and Catalysis Research Center, Chair of Technical Electrochemistry
Technical University of Munich
Lichtenbergstraße 4, 85748 Garching, Germany

delithiated state of the NCM cathode. As a result, batteries degrade more rapidly when consumers frequently maintain them in a fully charged state, such as when EVs are charged overnight. A study on charging patterns of EVs showed that of the averaged 23 h and 4 min of non-driving time per day a car is plugged into the socket for 16 h and 20 min.[5] This emphasizes the need for in-depth study of degradation at high potentials, where detrimental effects from high potentials[6–9] and cycling[10–12] are disentangled.

The main degradation mechanisms of modern high-Ni NCM cathodes include several key processes. First, i) the irreversible transition from the layered structure to a rocksalt-type (RS) phase results in a disordered surface reconstruction layer (SRL). Such SRL exhibits resistive properties at high potentials, i.e., high degrees of delithiation.[3,12–16] The phase transition is accompanied by the release of reactive (eventually singlet) oxygen,[11,17] which subsequently leads to: electrolyte decomposition[6,11,18–21] and ii) the formation of a cathode electrolyte interphase (CEI). Moreover, the CEI also forms as a result of chemical or electrochemical reactions occurring between the electrolyte and the CAM surface.[22,23] Additional degradation processes are iii) the dissolution/leaching of transition metal (TM) ions[24–26] into the electrolyte and iv) chemomechanical degradation caused by volume changes during de-/lithiation. The formation of cracks within the CAM particles can lead to loss of active material but also to increased active surface area.[13,14,27]

Oxygen release occurs at ≈80% delithiation independent of the specific CAM composition, which is ≈4.4 V versus Li^+/Li for NCM811[11,17,28] and results in a structural transition from layered Li_xTMO_2 to a cubic RS phase.[3,10,12–14,29] The SRL of NCM is believed to have a detrimental effect on cell cycling by increasing the charge transfer resistance[13,14,30] due to its electronically and ionically insulating nature.[12] This seems to be particularly relevant at high potentials, causing increased kinetic hindrance.[31]

Lattice oxygen released from the CAM at high potentials may partially form as highly reactive singlet oxygen,[17] which can then induce chemical oxidation of electrolyte.[11,18,32] The electrochemical decomposition of common organic electrolytes is believed to occur at potentials >4.9 V versus Li^+/Li.[6,32] Decomposition products can be gaseous or dissolved in the electrolyte[6,33–35] or they contribute to the formation of the CEI.[18,22] Traces of aluminum from the current collector,[35] cell casing or separator may also be integrated into the CEI. Crosstalk with the anode further influences the CEI composition.[36] Consequently, the composition and structure of the CEI depends on the specific cell configuration. Electrolyte additives promote the formation of a more stable CEI, protecting the CAM surface from severe side reactions.[23,37] The CEI typically comprises a layered nanostructure made up of organic and inorganic compounds. The latter include LiF, $Li_xPO_yF_z$, Al_xF_y and NiF_2, while organic compounds comprise $C_xH_yO_z$ and ROLi. The CEI formation is often associated with capacity loss due to increased resistance.[22,34,38–43]

Some detrimental effects during battery operation only emerge on full cell level, e.g., the loss of lithium inventory by side reactions occurring on the CAM at high potentials[29] or the crosstalk via dissolved TMs between the electrodes. TM dissolution itself only accounts for a comparably small loss of CAM, with a maximum reported loss of 0.45 wt.% over 100 cycles to 4.6 V versus Li^+/Li.[25,26,29,44] However, it significantly reduces capacity when dissolved TM ions deposit on the anode, causing unwanted behavior of the solid electrolyte interphase (SEI)[45] and potentially leading to lithium plating.[24]

This study reports on CAM related degradation mechanisms, namely i) structural degradation under oxygen release and ii) CEI formation, which are generally believed to occur at high potentials in the cathode. This is experimentally ensured by using an excess lithium reservoir (lithium metal anode) and 3-electrode cells with a gold wire reference electrode to separate impedance and overvoltage contributions from anode and cathode. We reduce the chemomechanical degradation, subsequent contact loss and changes in surface area of the CAM by selecting single crystalline (sc) NCM and minimizing cycling during cell operation. These issues are typically observed in polycrystalline secondary particles.[13,14,27] Our CAM focused approach enables us to gain insights into the temporal changes of the SRL and CEI during constant potential holds, setting our study apart from others that focus on varying cycling parameters or experimental conditions.[33,46]

We use a multi-analytical approach to examine the degradation of a commercial high-Ni CAM (NCM831106) after long holds at high potential (4.5 V versus Li^+/Li). All electrochemical potentials mentioned in this study are referenced against the Li^+/Li redox couple. The performance of the CAM is monitored via potentiostatic electrochemical impedance spectroscopy (PEIS) at various potentials over the course of the experiment (46 days at 4.5 V and a total runtime of 107 days). To track changes in CEI, we conduct *post mortem* analysis including X-ray photoelectron spectroscopy (XPS) and time of flight secondary ion mass spectrometry (ToF-SIMS) and Orbitrap-SIMS. These techniques provide surface-sensitive chemical information about the composition and thickness of the CEI. Transmission electron microscopy (TEM) is employed to determine the local crystal structure of CAM surface layers. We further employ a resistor network simulation to model inhomogeneous growth of SRL, offering a novel explanation for the previously unexplored phenomenon of non-linear increase in cathodic resistance. Our results provide a deep understanding of the structural and chemical degradation mechanisms in high-Ni NCM during prolonged high-potential holds. Moreover, we reveal the dominant contribution of the SRL over the CEI to the impedance of the cathode.

2. Results and Discussion

2.1. Electrochemical Measurements

In the electrochemical measurements, we selected a hold potential of $U_{hold} = 4.5$ V to investigate the degradation of NCM831106 during extended potential holds. This potential corresponds to ≈80% delithiation for the specific NCM, representing the onset of

T. Brezesinski, A. Kondrakov, J. Janek
Battery and Electrochemistry Laboratory (BELLA), Institute of Nanotechnology
Karlsruhe Institute of Technology (KIT)
Kaiserstr. 12, 76131 Karlsruhe, Germany
A. Kondrakov
BASF SE
Carl-Bosch-Str. 38, 67056 Ludwigshafen, Germany

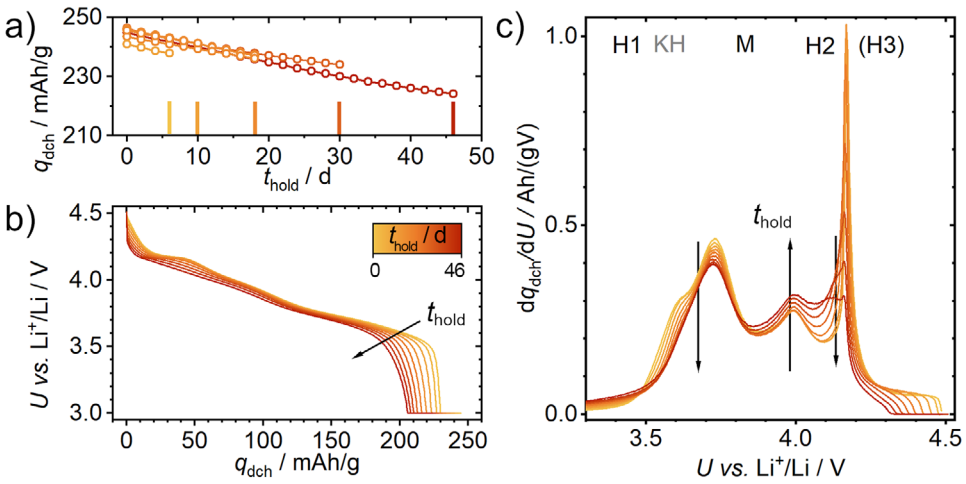

Figure 1. a) Discharge capacity of identical 3-electrode cells, stopped after various t_{hold} for *post mortem* analysis. The different colors indicate the maximum t_{hold} of each cell. Each point corresponds to a 0.1 C discharge including a 4 h potential hold at 3.0 V after a 2 d hold at U_{hold} = 4.5 V. b) Voltage profiles of discharges, with transient evolution denoted by color gradients and an arrow indicating increasing t_{hold}. (Not all discharges are shown for clarity) c) dq/dU plots of the discharge curves shown in Figure 1b. The arrows indicate the change in peak height over t_{hold}. The crystallographic single-phase regions are indicated in black, with H3 in brackets as the H2-H3 transition is suppressed and the kinetic hindrance region (KH) in gray.

oxygen release, while ensuring that electrochemical oxidation of the electrolyte is still negligible.[20] Each cell underwent a protocol consisting of 48 h at U_{hold}, a discharge and a consecutive charge including several impedance measurements at various potentials (details in experimental section). The total time a cathode was held at U_{hold} is described by the variable t_{hold}, which was 46 d for the longest protocol.

The NCM delivers a high initial specific capacity of 245 mAh g^{-1}, which decreases almost linearly to 224 mAh g^{-1} (0.1 C discharge from 4.5 to 3.0 V with a 4 h hold at 3.0 V) within 107 d of operation, including 46 d at 4.5 V as depicted in **Figure 1a** for six identical cells with different runtimes. In Figure 1b, the discharge curves (0.1 C) after subsequent high potential holds are shown.

The discharge profiles after the potential holds are almost unchanged at medium state of charge (SoC) within the first two weeks at 4.5 V, but show differences in the high potential (4.5 – 4.1 V) and the low potential region (3.7 – 3.0 V). Later, the capacity achieved during the potential plateau below ≈4.2 V shrinks. This plateau is associated with drastic changes along the c-axis (collapse or expansion) and is understood as a remnant of the H2-H3 transition known from $LiNiO_2$.[47] Also, the initial potential drop after the long potential hold increases. Additionally, the potential drop at 3.6 V occurs at lower specific capacities. These changes in electrochemical behavior can also be visualized in dq/dU plots, as shown in Figure 1c.

The kinetic hindrance peak (KH) at ≈3.6 V vanishes while the peak at 3.7 V (corresponding to the H1-M two-phase region)[3] is still visible but diminishes. The KH is attributed to the change from divacancy hopping mechanism across tetrahedral sites to single vacancy jump with a higher energy barrier at low vacancy concentration.[48,49] Interestingly the peak at ≈4.0 V and the region from ≈4.2 to 3.8 V are increasing in dq/dU due to smaller slopes between the plateaus in Figure 1b from 4.17 to 3.73 V. This can be explained by slow kinetics at the beginning of discharge, causing the capacity corresponding to the c-axis expansion below 4.2 V to be smeared out over a wider potential window. Additional electrochemical data, such as potential profiles during charge, total charges, Coulomb efficiency and average potentials are given in the Sections S1–S3 (Supporting Information).

To track the changes in electrochemical behavior of the degraded cathodes in more detail, impedance was measured at different potentials after each 48 h hold at U_{hold}. **Figure 2a–c** show the impedance spectra recorded at 3.7, 4.0 and 4.3 V, scaled with the mass of CAM to focus on material specific properties. Clearly, the impedance of the cathode depends strongly on potential, corresponding to a certain degree of lithiation. The EIS at 4.0 V shows two semicircles and a "tail" at low frequencies. The first semicircle is often attributed to high-frequency resistances, as, e.g., the contact resistance between the CAM and the current collector.[50] Its remarkable stability over 46 d at 4.5 V indicates strong and enduring contact within the cathode. The second semicircle with a characteristic frequency f_c of ≈50 Hz for 3.7 and 4.0 V after the first hold increases in resistance over the course of the experiment and f_c changes to ≈1 Hz. As this semicircle is changing with potential, it is attributed to the charge transfer process.[51] With a small charge transfer resistance (R_{CT}), a diffusion related impedance (visible in the tail) is observed at frequencies below 100 mHz. At 4.3 V, R_{CT} is already too high to observe the diffusion behavior from EIS in this frequency range. For 3.7 V, impedance was measured down to 100 µHz revealing the intercalant diffusion behavior, as shown in Figure 2a.

The impedance spectra were fitted using a simple R-(R)(P)-(R)(P) model, where a dash denotes a connection in series, brackets a connection in parallel and R and P stand for resistor and constant phase element, respectively. Figure S5 (Supporting Information) compares this simple equivalent circuit and an advanced transmission line model (TLM) to demonstrate that the simple model captures R_{CT} well. Figure 2d shows the increase in relative charge transfer resistance $R_{CT,rel}$ over t_{hold} at 4.5 V for the different measurement potentials. It is calculated from the absolute values of R_{CT}, normalized to the first recorded value, via

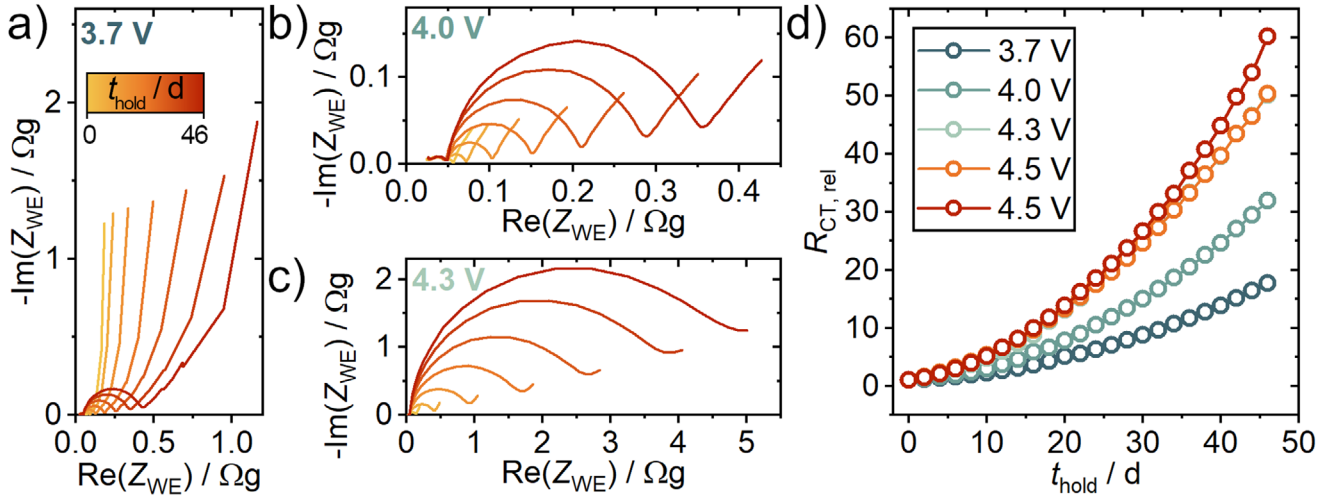

Figure 2. a) EIS data of the cathode impedance (Z_{WE}) at 3.7 V from 1 MHz to 100 µHz, b) at 4.0 V and c) at 4.3 V from 1 MHz to 100 mHz. The real and imaginary parts of Z_{WE} are given in Ωg_{CAM}, as they are scaled with the mass of active material (m_{CAM}) in the cathode. d) Relative increase of R_{CT} ($R_{CT,rel}$) determined by EIS measured at different potentials after holding steps. The orange curve is after 4 h at U_{hold}, the red one after 48 h. $R_{CT,rel}$ is calculated from the first recorded R_{CT} value and R_{CT} after t_{hold} via $R_{CT,rel}(t_{hold}) \equiv R_{CT}(t_{hold})/R_{CT}(t_{hold} = 0\ d)$. For the absolute R_{CT} values refer to Figure S4 (Supporting Information).

$R_{CT,rel}(t_{hold}) \equiv R_{CT}(t_{hold})/R_{CT}(t_{hold} = 0\ d)$. Please note that the absolute R_{CT} values at different potentials, given in the SI, vary by orders of magnitude, as shown exemplarily in Figure 2a–c. For all potentials a non-linear increase in R_{CT} is observed, while R_{CT} increases stronger when closer to the limits of the typical potential window. There is also an increase observed at the same potential before and after the long hold, as seen in the difference between the orange and red curve.

Typically, the increase in R_{CT}, often measured as direct current internal resistance (DCIR), is studied throughout cycling and is frequently described as linear.[4,13,52] However, the non-linear rise in resistance within cathodes has not been extensively explored in existing literature. Our analysis reveals that even for published studies, there is often an initial phase of slower, non-linear resistance increase over the first few hundreds of cycles, which then transitions into linear growth. The SI section S7 includes a collection of data from various studies, further illustrating this non-linear growth. In the SI section S4, we also argue that the increase in R_{CT} is not due to changes in SoC at a specified potential.

The strong potential dependence of R_{CT} is also shown in **Figure 3a**, where EIS was performed for another 3-electrode cell over the whole potential range at OCV after formation, after 46 days at U_{hold} and after harvesting the respective cathode, i.e., washing it with diethyl carbonate (DEC). Each measurement was conducted by reintroducing the same cathode to a fresh cell. The typical U-shape of R_{CT} as a function of OCV for layered Li_xTMO_2 is observed.[53,54] The induced degradation from the potential hold not only increases the R_{CT} values,[55] but also narrows the potential window, especially at high and low potentials.

Figure 3c shows the effective chemical diffusion coefficient $\tilde{D}_{Li}(x)$ of lithium as a function of lithium content x in Li_xNCM determined from the OCV relaxation curves after 10 min of 0.1 C pulses. As the OCV can be linked to the lithium concentration on the surface of the CAM (Coulometric titration), one can relate its decay after imposing a lithium concentration gradient in the CAM (e.g., via galvanostatic polarization) to the rate of diffusion inside the CAM. For this, an evaluation procedure previously published was applied.[56] We note that for such electrochemical diffusion measurements several strict assumptions and simplifications have to be made, which are discussed in the Section S8 (Supporting Information).

Surface changes, such as the formation of a degradation layer, affect $\tilde{D}_{Li}$, giving the impression of slower diffusion, while the bulk diffusion coefficient remains constant. Therefore, $\tilde{D}_{Li}$ values from electrochemical measurements have to be understood as effective, averaged values and can indirectly hint toward a degradation layer or inhomogeneous delithiation, for example.[57] Comparing $\tilde{D}_{Li}$ of the pristine cathode with the one held at 4.5 V reveals a severe decrease over the whole SoC range (again stronger at low and high potentials). The washed cathode reveals a similar behavior except from 4.0 to 4.5 V, where it shows a particularly low $\tilde{D}_{Li}$, and below 3.7 V, where $\tilde{D}_{Li}$ is also smaller. The similarities of the curves indicate that the washing procedure to remove salt residues from harvested cathodes before *post mortem* investigation is not altering their properties. Therefore, we assume that electrolyte decomposition or salt depletion do not play an important role in the present study. It rather highlights that changes of $\tilde{D}_{Li}$ and R_{CT} can be attributed to CAM-related degradation effects.

Summarizing the electrochemical results, long potential holds lead to a slow, rather linear capacity decay, while the charge transfer resistance measured at a given potential increases nonlinearly, depending on the potential. From the charge curves we conclude that long potential holds mainly affect the CAM performance kinetically and do not significantly decrease the bulk capacity of the material in the investigated time period. The values of R_{CT} and $\tilde{D}_{Li}$ as a function of SoC before and after calendar aging at U_{hold} further underline this. Especially the regions at high and low degrees of lithiation, where charge transfer and diffusion are already slow in the pristine state, are affected most.

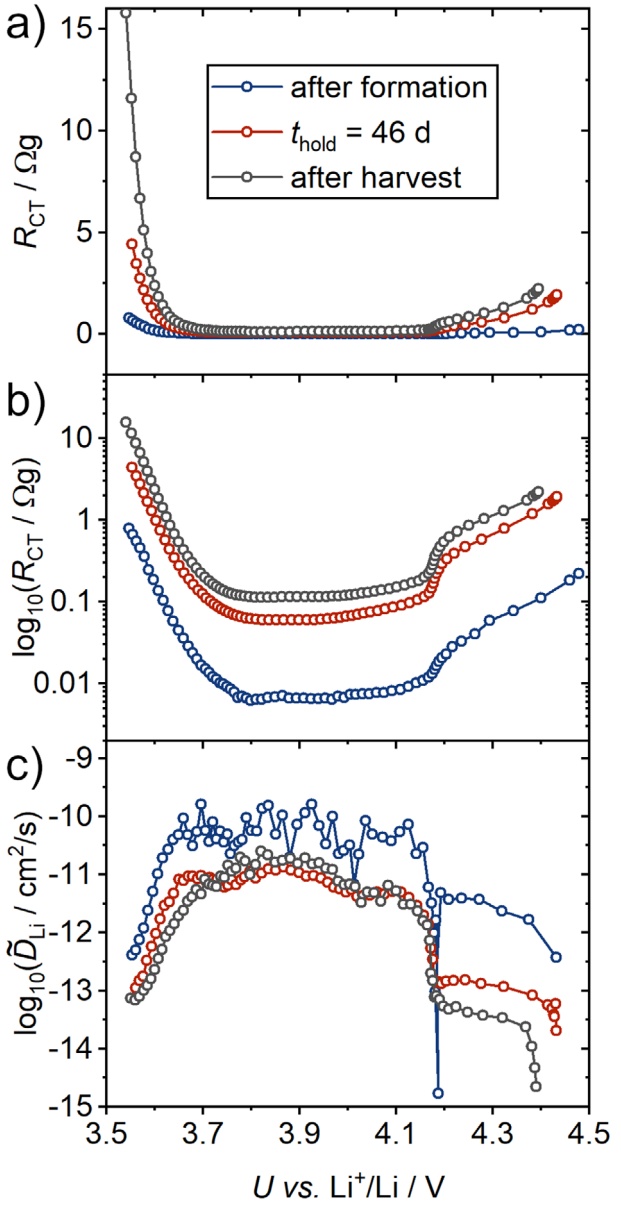

Figure 3. a) Charge transfer resistance R_{CT} (determined via fitting impedance spectra 1 MHz – 100 mHz) measured after 2 h OCV at different SoC for: Pristine cathode (blue), after 46 d hold at 4.5 V (red), measured with a new anode and reference electrode, and finally, after harvesting the cathode and washing it with DEC (gray). The resistances are normalized to g_{CAM}. b) R_{CT} curves on logarithmic scale for better readability. c) Effective chemical diffusion coefficients of lithium in the CAM, as determined from OCV relaxation after 0.1 C pulses for 10 min, as described in the Section S8 (Supporting Information).

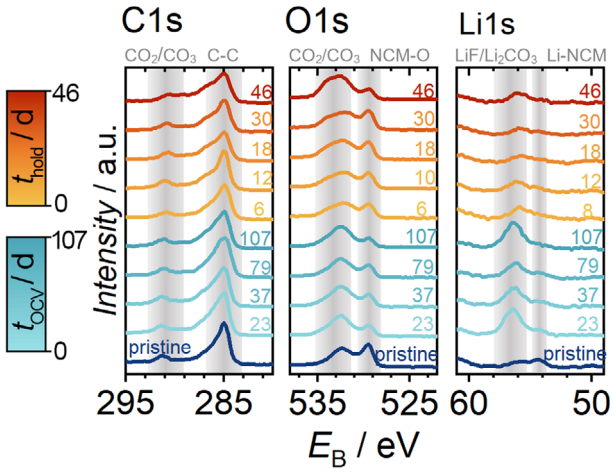

Figure 4. XP detail spectra for a) C 1s, b) O 1s, and c) Li 1s. Spectra collected from the pristine cathode (bottom, dark blue), cathodes stored at OCV for up to t_{OCV} = 107 d (turquoise), and those held at U_{hold} for up to t_{hold} = 46 d (yellow to red) are displayed. The numbers next to each curve indicate the exact t_{OCV} or t_{hold} for the respective cathodes.

What is the reason for the kinetic hindrance? In several studies, an increase in cathode impedance is explained by a decrease in surface area or mass loss of CAM, e.g., due to cracking.[56] Several of our observations do not agree with that. First, the bulk capacity is not decaying in the same way as R_{CT} is increasing, ruling out substantial mass loss. Additionally, the liquid electrolyte and NCM interface (LE|NCM) area typically increases during operation, which would decrease $R_{CT,}$ as shown by physisorption and electrochemical measurements.[56,58] Second, the degradation not only increases R_{CT}, but also changes the potential dependence. This hints toward a more complex mechanism. More likely, the LE|NCM interface is degrading.[30,53] After SRL and CEI formation on the CAM surface, the system is better described as LE|CEI|SRL|NCM.

Using online-electrochemical mass spectrometry (OEMS),[59] we demonstrate that both structural degradation of CAM, due to lattice oxygen release, and chemical oxidation of the electrolyte occur simultaneously when reaching 4.5 V. The OEMS data are presented in the Figure S10 (Supporting Information). These processes likely contribute to the observed nonlinear increase in impedance over t_{hold}. The SRL is known to have lower electronic and ionic conductivities[12–14,30,31] and the CEI is also considered to have low electronic conductivity while allowing for Li^+ transport.

2.2. Chemical Composition of the Cathode Electrolyte Interphase

To correlate the changes in CEI with the observed increase in R_{CT}, cells held at U_{hold} for different t_{hold}, as shown in Figure 1a, were analyzed *post mortem*. Additionally, reference cathodes were examined. This includes a pristine cathode that was only exposed to the DEC washing solution (referred to as "pristine") and cathodes that were stored at OCV up to t_{ocv} = 107 days (referred to as "OCV") corresponding to the total runtime of cells held at U_{hold}.

To track changes in chemical composition of the CEI, XPS and ToF/Orbitrap-SIMS were used. In **Figure 4**, the C 1s, O 1s, and Li 1s detail spectra are presented for all cathodes. The data are normalized to the maximum intensity, with an offset added for better visibility. Evaluation of the XP spectra was done on the basis of several publications about NCM degradation.[7,15,22,33,34,46] The F 1s, P 2p, and Ni 2p detail spectra are given in the Figure S11 (Supporting Information).

Comparing the C 1s spectra of the pristine, OCV, and cathodes held at U_{hold} = 4.5 V, the intensity of the C-C peak

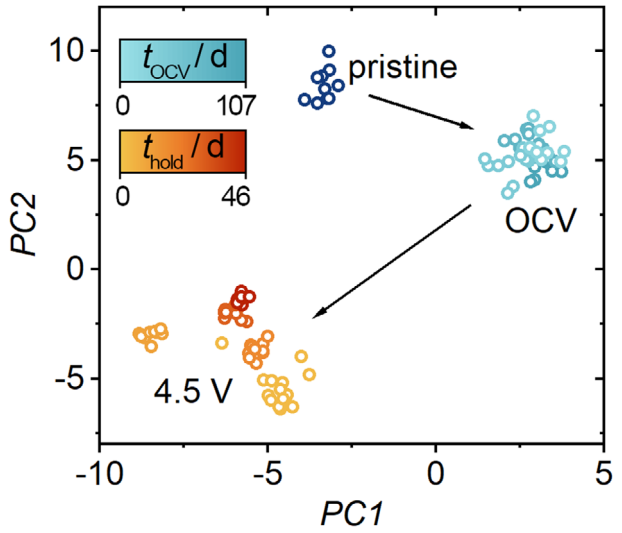

Figure 5. Principal components 1 and 2 from the PCA results of the ToF-SIMS surface spectra of the pristine (blue), OCV for various t_{OCV} (turquoise) and cathodes held at U_{hold} for various t_{hold} (yellow to red).

decreases relative to the signals at higher binding energies (up to E_B = 292.0 eV). This indicates an increase in oxidized carbon species on the cathode surface. A similar trend is observed in the O 1s spectra, where the shoulder at E_B > 533.0 eV (labeled CO_2/CO_3) becomes more pronounced, which is also an indication that PO_xF_y species are formed. Additionally, the signal at E_B = 529.5 eV, corresponding to the TM-O bond in NCM, is present in all spectra. Given the photoelectron escape depth of maximum 10 nm, this suggests that the CEI on these cathodes is thinner than 10 nm. In the Li 1s spectra, intercalated lithium is visible as well (E_B = 54.5 eV). Furthermore, the spectra demonstrate that the LiF content in the CEI is higher for OCV cells compared to cathodes held at U_{hold}.

This suggests that already during cell assembly, the electrolyte undergoes degradation, forming a CEI on the cathode, which is primarily composed of LiF and organic compounds ($C_xH_yO_z$). When the cell is held at U_{hold}, the CEI composition changes, with a decrease in LiF content and an increase in oxidized organic species ($C_xH_yO_z$ and C_xH_yOLi), but the overall amount of organic species decreases. It has been reported that during cell cycling LiF, $C_xH_yO_z$, C_xH_yOLi, Al_xF_y, $Li_xPO_yF_z$ and NiF_2 are formed on the surface of the CAM.[7,15,22,33,34,46] Using XPS, we were unable to detect any formation of Al_xF_y or NiF_2. In our case, the analyzed cathodes show less $Li_xPO_yF_z$ compounds in the XP spectra compared to literature, which may be due to different cell setups or sample preparation, e.g., washing.[33,34]

When combined with the XPS data (revealing the chemical environment of elements in the CEI), ToF-SIMS surface spectra can be used to gain a better understanding of how the CEI evolves over time. The score plot of a principal component analysis (PCA) of those spectra is shown in **Figure 5**. There is a clear difference in chemical composition of the different cathode surfaces. This indicates that the cathodes have unique CEI compositions based on their electrochemical history (pristine, OCV, U_{hold}).

Next, the loadings (Figure S13, Supporting Information) from the component plot of Principal Component 1 (*PC1*) and 2 (*PC2*) of the ToF-SIMS surface spectra were evaluated. The pristine sample is characterized by signals primarily originating from NCM, such as NiO_2^- and NiO^- secondary ions, as well as impurities from NCM (e.g., Cl^-, $Li_2CO_3^-$ secondary ions) and other cathode components (binder and carbon). When the cathode is stored at OCV without prior cycling, the CEI evolves, containing more organic residues from the electrolyte solvent, along with an increased deposition of LiF on the surface, in agreement with the XPS observations. This results in a decrease in NCM signal, suggesting a thicker CEI layer. There is no clear indication of compositional changes with extended storage at OCV, as the PCA component plot shows little difference between the different OCV samples. This suggests that during OCV storage, a stable CEI is formed on the NCM.

In contrast, cathodes held at U_{hold} produce a distinct cluster in the PCA component plot and differences among various t_{hold} at U_{hold} are also apparent. This provides clear evidence that the chemical composition of CEI evolves with t_{hold}. The main difference between OCV and 4.5 V cells is the increase in fluorine compounds (e.g., NiF_2^-), oxidized electrolyte solvent (e.g., $C_2H_3O_2^-$), oxidized conducting salt (e.g., $LiPO_3F^-$), and oxidized aluminum foil (e.g., AlF_4^-). In contrast, the signals from LiF_2^- and organics (e.g., $C_2H_3^-$) are decreasing. These changes in the CEI's chemical composition lead to a relative increase of the CAM signals, indicating that the surface layer becomes thinner compared to the OCV cells. Alternatively, this observation could be explained by a CEI that covers less of the CAM.

To investigate the depth-resolved chemical composition of the CEI, Orbitrap-SIMS analysis was performed. Its layered nanostructure poses a challenge when measuring depth profiles, as the sputter yield depends strongly on the material (matrix). In general, organic compounds are more prone to sputtering than inorganic ones, meaning that they are removed more quickly during depth profiling in the SIMS analysis. **Figure 6** shows the depth profiles for pristine, OCV, and t_{hold} = 46 d. The signal intensity is normalized to the maximum intensity of the plotted fragments for better comparison of depth profiles. The raw maximum counts are provided in the Table S4 (Supporting Information). The NiO_2^- signal represents the NCM, while three other signals represent different degradation products within the CEI: NiF_2^- forming through side reactions of NCM with the electrolyte, $AlO_2H_2F_2^-$ from degradation of the aluminum current collector and electrolyte, and $C_2H_3O_2^-$, which is a degradation product of the electrolyte.

When comparing the depth profiles for pristine (Figure 6a) and OCV cathodes (Figure 6b), we find a thicker CEI of the latter, consisting of an outer organic layer that is quickly removed due to its higher sputtering rate. The inner, inorganic layer contains degradation products from the aluminum current collector ($AlO_2H_2F_2^-$) and CAM (NiF_2^-), until the CAM signal reaches its maximum. In contrast, the pristine sample shows only minor impurities with significantly lower fragment intensity compared to the OCV sample. For cathodes maintained at U_{hold} = 4.5 V (Figure 6c), the CEI thickness decreases compared to that at OCV. Moreover, there is an increase in the overall NiF_2^- and $AlO_2H_2F_2^-$ contents, indicating an enrichment of these fragments within the CEI. This observed increase in the $AlO_2H_2F_2^-$ fragments indicates that degradation products from the current collector integrate into the CEI, which is not previously reported.

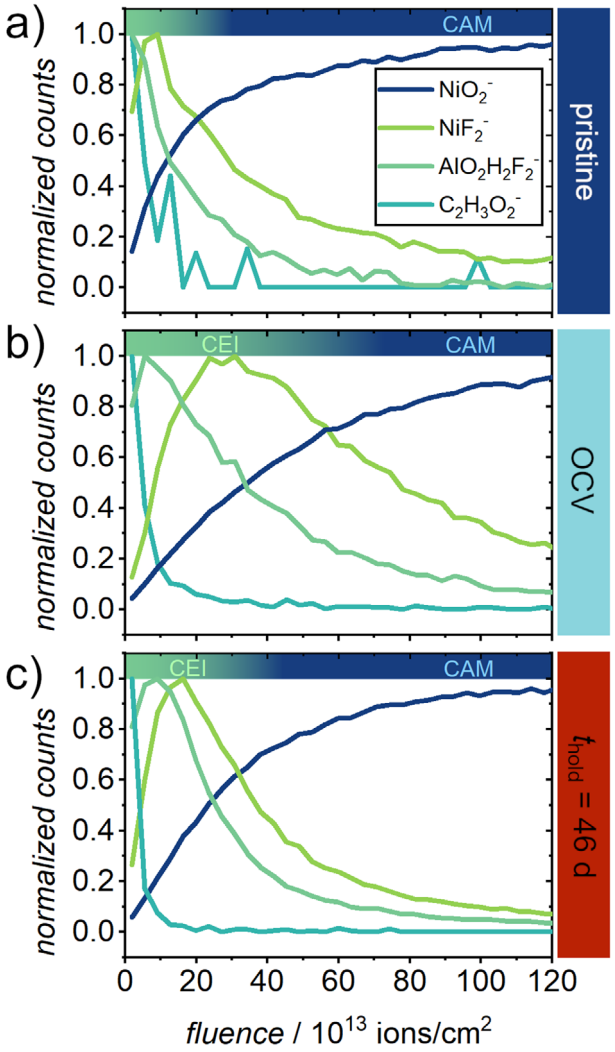

Figure 6. Orbitrap-SIMS depth profiles for the cathode surfaces: a) pristine, b) OCV, and c) held at U_{hold}. The analyzed ion fragments include NiO_2^-, NiF_2^-, $AlO_2H_2F_2^-$, and $C_2H_3O_2^-$. The fluence is indicative of the depth within the sample. Absolute counts are given in Figure S14 (Supporting Information).

In summary, surface analysis by XPS and ToF/Orbitrap-SIMS reveals that the CEI begins to form immediately upon contact between electrolyte and NCM. This initially formed CEI remains chemically stable during calendar aging and consists of multiple layers, an outer layer dominated by organic species and an inner layer composed of inorganic species, aligning with other studies on cycled cells.[22,42] When the cathode is charged to 4.5 V and held at this potential, the CEI composition changes. Specifically, the content of LiF and organic species decreases ($C_xH_yO_z$), resulting in a thinner CEI that accumulates additional fluorinated compounds originating from both the aluminum current collector and the NCM (Al_xF_y, NiF_2), as well as oxidized species from the electrolyte solvent and conducting salt ($C_xH_yO_z$, $Li_xPO_yF_z$). Longer application of U_{hold} then only leads to slight intensification of these effects. Higher cut-off potentials and elevated temperature are known to increase the formation of degradation products.[6,7,33,34,41,46] Notably, the evolution of the CEI is dynamic and depends on the electrochemical history of the electrode.[23,60–64]

Clearly, holding the cathode at high potential reduces the CEI thickness and alters its relative composition compared to the OCV state, which has not been reported so far. Previous studies by Yu et al. and Luo et al. discuss the reduction of CEI thickness for Ni-rich NCMs, when going from 4.1 to 4.8 V.[33,46] This thinning effect is likely due to the release of singlet oxygen, which reacts with the CEI and forms degradation products that dissolve into the electrolyte,[33,34] and higher reactivity of Ni-O bonds of the CAM at lower Li contents.[46] Interestingly, the minimal compositional variations in the CEI and its constant thickness observed during prolonged holding at U_{hold} suggest that the increase in impedance is not directly associated with changes in CEI.

2.3. Structural Degradation

To explore whether structural degradation of surface layers contributes to increased kinetic hindrance after long voltage holds, high-resolution scanning TEM (HRSTEM) was performed on cathodes after various t_{hold}. HRSTEM allows imaging with atomic resolution, thus it is a powerful technique for highly localized analyses.[65] For the investigations, the high angle annular dark field (HAADF) method was employed, which is characterized by a pronounced Z-contrast, resulting in the fact that Li^+ positions can readily be distinguished from those of heavier cations.

For the measured samples in this study two main observations stand out: First, with increasing t_{hold} an expanding phase near the CAM surface is observed, as shown in **Figure 7** from left to right. This phase is attributed to a cubic, rocksalt-type phase ($Fm\bar{3}m$ space group), which is well documented in numerous previous reports and likely exhibits stoichiometries close to TM_1O_1, with x being small in $Li_xTM_{1-x}O_1$, where TM can be Ni, Co, or Mn.[14,16] The increase in thickness of the RS phase is only significant when comparing particle surfaces that are accessible (lithium layers perpendicular to the c-axis, so intercalation layers are "open" toward the electrolyte), as notable when comparing the images in Figure 7 from top ("open") to bottom ("closed").

Second, there is a gradual transition in the SRL from layered to the RS structure with many local inhomogeneities and strong variations along the surface of particles. It should be highlighted that harvested cathodes showed variations in SRL thickness, even for individual CAM particles. Especially when the particle had open interfaces to the electrolyte, instead of other particles in its surrounding, the degradation layer showed increased thickness. This is further supported by another HAADF-STEM image of two sides of a degraded CAM particle as well as by electron energy loss spectroscopy (EELS) in Figures S15 and S16 (Supporting Information). Additionally, we note that in one sample with t_{hold} = 46 d, cracking along the lithium layers, and corresponding layer gliding occurred, as illustrated in the Figure S17 (Supporting Information). Naturally, also a SRL was observed on these newly formed surfaces.

Irrespective of inhomogeneities and anisotropic growth of the RS phase, its increase in thickness is correlated with t_{hold} in the presented measurements. This phase is the result of an irreversible transition after oxygen release and caused by

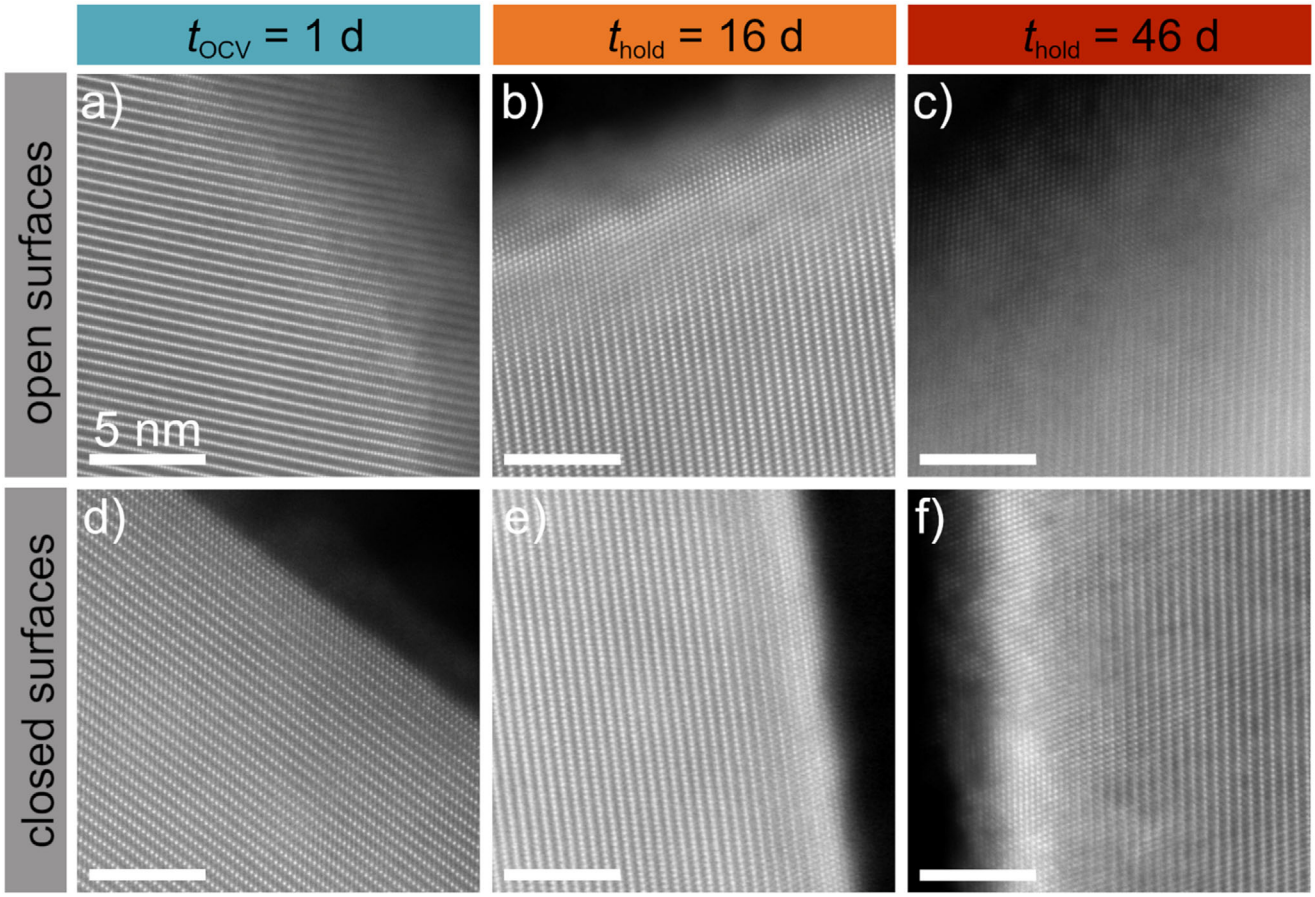

Figure 7. HAADF-STEM images of lamellas from harvested cathodes. For three selected samples (from left to right) "open" and "closed" surfaces of the same cathode are shown (in the top and bottom, respectively). The first cathode rested for 1 d at OCV. The other two samples underwent the hold procedure at 4.5 V for various t_{hold}. a,d) t_{OCV} = 1 d,b,e) t_{hold} = 16 d and c,f) t_{hold} = 46 d.

strong delithiation at high potentials, as also described in literature.[14,16,66] The "open" surfaces with access to lithium layers are the preferred interfaces for charge transfer from the electrolyte into the CAM. These regions undergo more rapid and pronounced changes in lithiation, eventually resulting in more severe degradation, compared to "closed" surfaces, where Li^+ must cross the close-packed basal plane in the layered structure. Consequently, the extent of degradation depends strongly on the local orientation of the respective crystal surface, as also reported elsewhere.[15]

However, the non-uniform growth of the RS phase requires discussion, since it appears to deviate from literature, often reporting a rather defined layer thickness.[12,15,40,67–69] There, the rocksalt-type phase and sometimes a transition layer are visually separated with straight lines from the layered bulk in the HAADF-STEM images. Inhomogeneous RS phase growth, however, has been partly described by Ko et al., Jung et al. and briefly mentioned by Lin et al. and Schweidler et al., all in studies with cycled cathodes.[4,12,14,15] A recent work by Lun et al. also highlights the detrimental effect of uneven RS phase coverage on the diffusion properties of NCM.[57] Here, we use a novel approach to visualize this phenomenon, by constructing a phase map from a HAADF-STEM image, utilizing the crystallographic differences visible in the Fourier spectra to distinguish between the layered and RS phase. The result is presented in **Figure 8**. For the construction of this map, the image is divided into unit-cell-sized patches on which a fast Fourier transform (FFT) is applied. The patches are then classified into RS phase, transition boundary or layered structure based on the ratio of Fourier coefficients of RS and layered phase. It is important to note that throughout our TEM analyses of the degraded cathodes, no distinct regions attributable to a spinel-like phase were identified. This suggests that for this Ni-rich NCM, the layered structure appears to transform directly to a rocksalt-like phase.

The map clearly shows how the degradation of the layered structure occurs gradually and how the RS phase is distributed locally. This gradual transition is typical for epitactic and coherent phase growth and enables the partial occupation of lithium sites by TM-ions ($Ni_{Li}^{\bullet}$). In fact, this makes the determination of one specific value for the thickness of the degradation layer obsolete and any quantitative measure of SRL thickness will be an apparent and averaged thickness.

A reason for the more gradual transition from layered to RS phase in our cathodes, compared to long-term cycling studies, may be the calendar aging protocol, where high potentials are applied continuously but repeated phase transitions or lattice

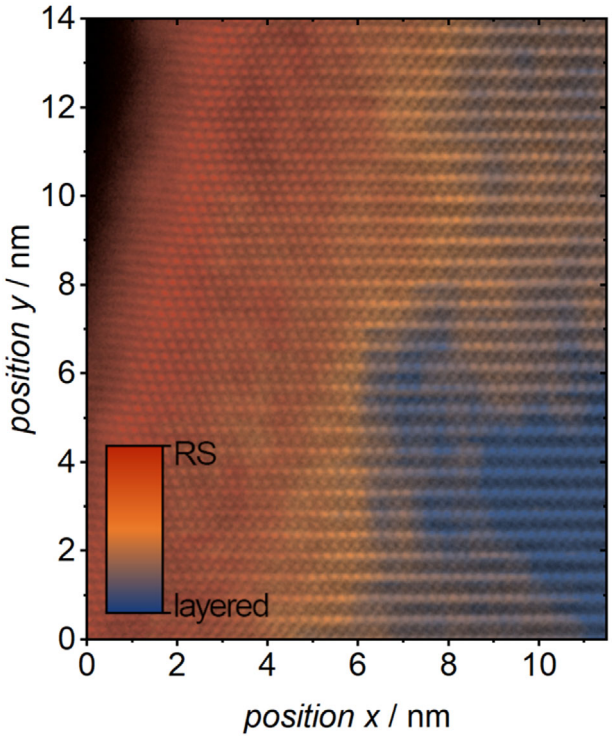

Figure 8. Fourier coefficient mapping ("phase map") of a HAADF-STEM image (sample aged at 4.5 V for t_{hold} = 16 d). A non-uniform reconstruction layer (SRL) and a gradual transition between layered and RS phase are observed.

contractions, e.g., the c-axis collapse when charging above ≈4.1 V, are avoided. This layer collapse is believed to be one of the main factors leading to CAM loss and kinetic hindrance due to RS phase formation.[3,11,70] A more detailed comparison of aging with and without cycling is object of ongoing investigation.

In general, the presence of homogeneous degradation layers in particles of a complex, 3D porous cathode system with inhomogeneous delithiation and preferred current paths, seems unlikely, even when using very thin cathodes. This applies to both the electrode and particle levels.

To summarize, the trend of growing RS phase on the CAM surface with prolonged exposure at high potentials is confirmed for "open" surfaces. The evolution of the degradation layer is following anisotropic growth from surface to bulk that is disturbed by the local environment, defects and inhomogeneities, resulting in a non-uniform thickness. In the following, we will show that the observed growth of SRL may explain the nonlinear increase in cathode resistance.

2.4. Resistor Network Simulations

The ionic and electronic partial conductivities of the SRL are assumed to be low, and often understood as cause of kinetic hindrance.[12–14,30,31] To probe the influence of the inhomogeneous distribution of a phase with higher resistance along the CAM surface, we created a resistor network model with minimal input parameters. In the model, resistors of two magnitudes (R_{RS} = 1000, $R_{layered}$ = 1) are connected in a grid to simulate a small volume (26 × 51 × 51 voxels) of CAM, as shown in Figure S18 (Supporting Information). A potential difference is applied across the CAM volume, i.e., from left to right in the 2D projection in **Figure 9**a–d. Here the left side corresponds to the LE|NCM interface and the right side represents the CAM bulk. Voxels that experienced the highest local current were then switched from $R_{layered}$ to R_{RS} iteratively in each simulation step, thus modeling the gradual reconstruction of the layered phase. Already with minimal input parameters, we were able to simulate a nonlinearly growing total resistance R_{tot} due to an inhomogeneously growing resistive phase. In Figure 9a–d, the structural evolution of the simulated volume is depicted. Figure 9e shows the corresponding R_{tot}.

As initial configuration in Figure 9a, 5% of the resistances were set to R_{RS} (red voxels) in the five left layers of the grid, to represent the degraded CAM surface under OCV conditions (see Figure 7d). The rest of the CAM is in the pristine, layered state (blue voxels). Consequently, the voxel colors in Figure 9 range from the layered phase (blue) to the RS phase (red), as depicted by the color bar. This gradient results from interpolating/projecting the average voxel values (1 for RS, 0 for layered) along the z-direction. By using the partial currents to switch local resistances from $R_{layered}$ to R_{RS} we aim to model a phase reconstruction caused by delithiation as observed in the conducted hold experiments. For the simulation in Figure 9, β = 10 voxels are selected to switch from $R_{layered}$ to R_{RS} from the top 10% (γ = 0.1) of voxels with the highest partial currents. This is done using a probability-weighted random method, where the probability of each voxel being switched is proportional to its current magnitude relative to the sum of the top 10% highest currents. The formation of a degradation layer as shown in Figure 9a–d is influenced by the initial configuration, the resistance ratio $\alpha = R_{RS}/R_{layered}$, the number of voxels β "degrading" in each iteration and the probabilistic element γ. Further details regarding the setup and parameter studies are given in the Section S15 (Supporting Information).

The evolution of the total resistance R_{tot} of the modeled region, as shown in Figure 9e, can be divided into two regimes. The first one, here denoted as *constriction* regime, shows nonlinear growth with an increasing slope. This occurs while there are still paths from left to right with only "layered" voxels that get increasingly narrow until a covering plane of RS phase spans in the plane parallel to the surface. The current has then to cross this continuous resistive RS layer as shown in Figure 9c. Then, an approximately linear growth of R_{tot} sets in as the degradation layer extends in thickness but is still preserving inhomogeneities (Figure 9d). This resistance growth, with its nonlinear initial and later linear behavior, exhibits a similar shape compared to the experimental observations in Figure 2d. Also, the microstructure formed after several simulation iterations reveals similar degradation layers when compared to the phase map in Figure 8.

The simulation of the complex physics and chemistry of charge transfer into degrading CAMs is possible within our simple model with several simplifications. First, it compares the ionic transport of charge through the surface layers, so it neglects all processes in the electrolyte (stripping of solvation shells of Li^+ etc.). Furthermore, diffusion of formal, neutral lithium inside the CAM is neglected since it becomes rate-controlling at longer times/lower frequencies, as seen in Figure 2a–c. Also, the model

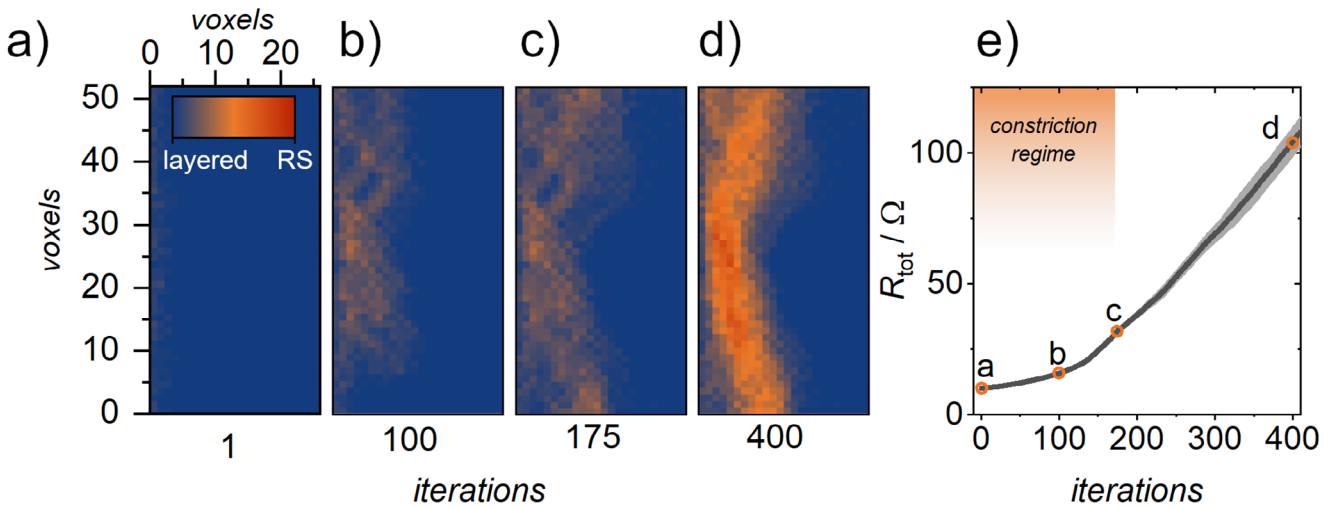

Figure 9. a–d) Visualization of a resistor network after several iterations showing inhomogeneous growth of the RS phase. Voxels are colored red when all 51 voxels in the (projected) non-visible z-direction are set to $R_{RS} = 1000\ \Omega$ and blue for $R_{layered} = 1\ \Omega$. Intermediate colors are interpolated when only a fraction is set to R_{RS}. Voxels switch from $R_{layered}$ to R_{RS} when they experience higher local currents after an applied potential difference between left and right edge (modeling the electrolyte interface and the CAM bulk, respectively). e) The total resistance R_{tot} increases nonlinearly in the *constriction* regime until a full coverage in the plane parallel to the surface is reached. Then, linear growth isobserved. Orange circles indicate the simulation steps shown in a-d). The error from 3 simulations is shown in grey and the line corresponds to the average R_{tot}.

extrapolates the behavior of a cuboid volume to the complex geometry of a 3D porous cathode. The fourth simplification is the assumption of an isotropic model. Clearly, ion and electron transport in layered materials show anisotropic characteristics, yet we assume that this will not cause qualitative changes to our model.

2.5. Derived NCM Degradation Mechanism and Implications for Other Layered Oxides and Full Cells

With the insights gained from the electrochemical experiments, the multi-analytical investigation and the resistor-network simulations, we derived a schematic picture of the dominant degradation processes and the resulting SRL and CEI during long potential holds, as shown in **Figure 10**.

The first contact of CAM with electrolyte already induces formation of a CEI primarily consisting of organic compounds ($C_xH_yO_z$) and LiF, with minor traces of $C_xH_yO_z$, C_xH_yOLi, $Li_xPO_yF_z$ and NiF_2. This CEI decreases in thickness after CAM exposure to high potentials, by reducing the contribution of organic species ($C_xH_yO_z$) and LiF. Simultaneously, minor increases in more oxidized organics ($C_xH_yO_z$, C_xH_yOLi) and accumulation of inorganic compounds (NiF_2, AlF_x, and $Li_xPO_yF_z$) can be observed, leading to a more distinct layered nanostructure. These AlF_x fragments originate from the current collector and integrate into the CEI, a phenomenon not previously reported. These changes become more pronounced for longer t_{hold}, though they remain minor compared to the changes from OCV to U_{hold} cathodes. Even the OCV cathode shows small regions of a structurally degraded phase ($Ni^{\bullet}_{Li}$ or RS phase) along the CAM surface layers in contact with the electrolyte. After prolonged application of high potentials, these regions grow under oxygen release. This growth of the SRL correlates with an increase in cathode impedance. The observed stability in the composition and structure of the CEI suggests the RS phase is the primary contributor to this resistance increase. However, the possibility of local inhomogeneities within the CEI causing additional constriction effects cannot be excluded. The non-uniform growth of the SRL creates tortuous paths for Li^+ toward the CAM bulk. Current constriction effects around these inhomogeneous, gradual transition regions lead to nonlinear increase of the overall cathode impedance. Another consequence is the inhomogeneous delithiation of CAM particles, resulting in severe capacity loss when applying high currents, as shown by Lun et al.[57]

How Applicable are the Results of Our Study to Other Materials and Cells?

Operating high-Ni NCM, such as NCM831106, at potentials as high as 4.5 V versus Li^+/Li exceeds typical upper cut-off limits for practical applications. Our study employed such conditions to probe fundamental degradation mechanisms. This can also be understood as an accelerated calendar aging at high potentials.[6] The observed formation of an inhomogeneous, resistive SRL over time and its correlation with non-linear impedance growth are phenomena we believe to be broadly applicable to NCM and other layered cathodes that degrade via rocksalt-like surface reconstruction, particularly those with high Ni content (e.g., > 50%). A lower Ni content and/or lower potential would primarily alter the rate, and therefore the extent, of structural degradation at the NCM surface, implying that this degradation mechanism is expected to be a common feature in these materials.

Furthermore, this study utilized half-cells with a lithium metal anode, an Au-wire reference electrode and an electrolyte without additives. This experimental design intentionally isolated intrinsic CAM degradation mechanisms by excluding anode-related phenomena (e.g., crosstalk with the graphite anode) and the influence of electrolyte additives. Consequently, while the direct quantitative transfer of these results (e.g., specific degradation rates or impedance values) to commercial Li-ion full cells may be

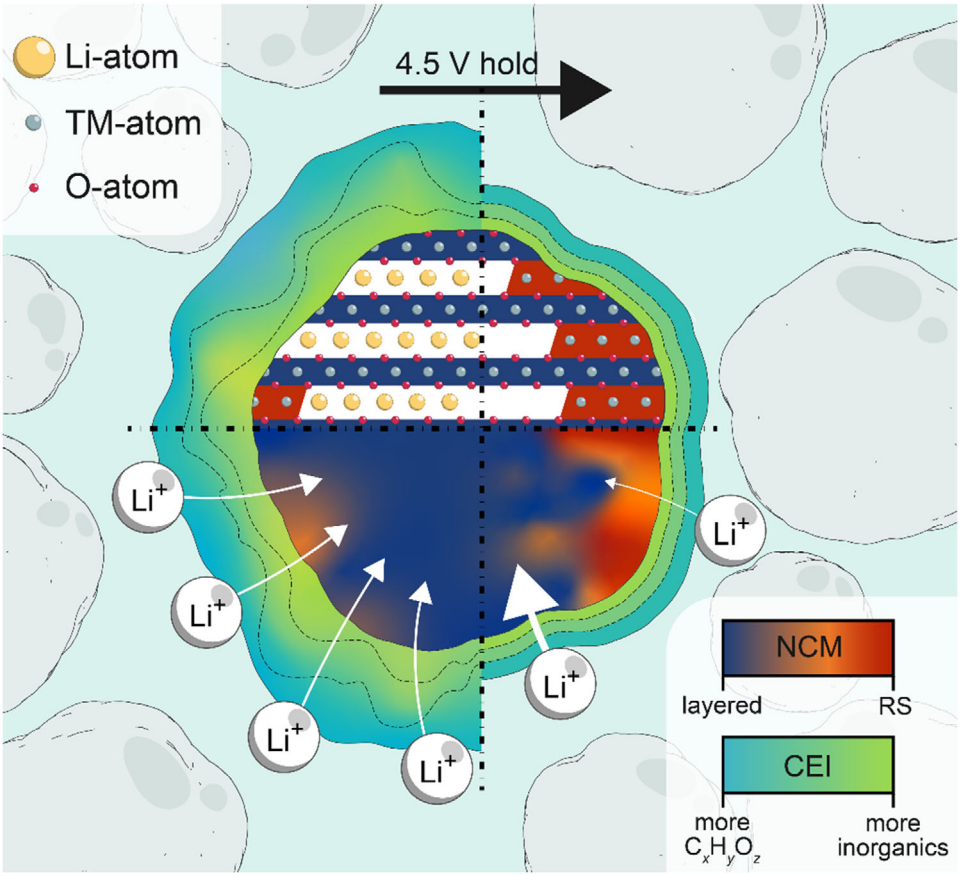

Figure 10. Schematic showing the effect of prolonged application of high potentials on the LE|NCM interface. The CEI thickness decreases and the layered phase of the CAM is irreversibly reconstructed under the release of oxygen. The inhomogeneous formation of this resistive, rocksalt-type phase leads to constriction effects that increase the cathode resistance nonlinearly with time. Credit: Elisa Monte/JLU Giessen.

limited, the fundamental understanding gained still applies. The identified inhomogeneous SRL formation over time and, therefore, the contribution to the rise in charge transfer resistance due to constriction provides a foundational baseline necessary for interpreting the more complex interplay of degradation factors in practical full-cell systems. Further investigations are needed to explore these multifaceted contributions in full-cell systems.

3. Conclusions

Detailed electrochemical investigations and multi-method *post mortem* analyses were performed on single crystal NCM831106 cathodes exposed to long constant potential holds at $U_{hold} = 4.5$ V versus Li^+/Li. The main detrimental effects are of kinetic nature, especially at high and low potentials, where also pristine, layered TM oxides show slow lithium kinetics due to both high charge transfer resistance and poor diffusivity. The charge transfer resistance of the cathode is increasing nonlinearly with prolonged time at high potentials. This is correlated to an inhomogeneous, gradual growth of a rocksalt-type phase, mainly for regions with "open" CAM surfaces, as revealed by structural analysis via TEM. The XPS and SIMS analyses reveal that, following initial thinning, the composition and structure of the CEI remains stable during prolonged holds with only subtle changes. Based on a novel TEM image processing technique and resistor network simulations, we present a simple model for nonlinear resistance growth caused by a proposed constriction mechanism. This constriction effect arises from the inhomogeneous distribution of high-resistive rocksalt-type regions near the CAM surface, which leads to preferred charge-transfer paths. Our study provides valuable insights into the temporal evolution of the CEI and SRL under high-voltage conditions. These findings contribute to a more fundamental understanding of CAM degradation, highlighting the critical role of SRL in contrast to the less decisive influence of the CEI.

4. Experimental Section

Cathode Preparation and Cell Construction: Single crystalline $LiNi_{0.83}Co_{0.11}Mn_{0.06}$ (MSE Supplies LLC, Tucson, USA) was used as CAM. The powder has a specific surface area of (0.61 ± 0.01) $m^2\ g^{-1}$, as measured by Krypton BET and an approximate mean particle size of 1 µm, as estimated from SEM images. Acid titration of the pristine NCM powder indicate 0.34 wt% of LiOH on the material surface, with no detectable Li_2CO_3 residuals. XPS survey scans of the as-received material revealed the presence of a zirconium doping and a borate coating.

To prepare electrodes, the CAM was mixed with NMP (Sigma–Aldrich Chemie GmbH, Steinheim, Germany), SuperP Carbon (MSE Supplies LLC, Tucson, USA) and PVDF (Arkema France, Colombes Cedex, France) under

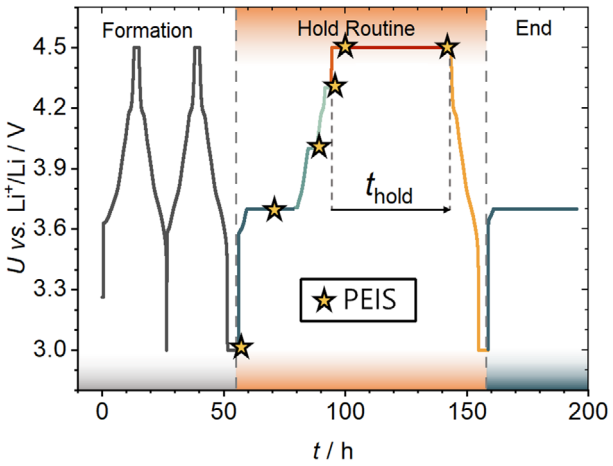

Figure 11. Schematic of the applied electrochemical procedure. All galvanostatic charge steps were performed at 0.1 C, corresponding to 200 mAh g^{-1}. Left side: Formation from 3.0 – 4.5 V including a 2 h hold at 4.5 V and a final 4 h hold at 3.0 V. Middle: Hold routine starting with PEIS1 (see text for detailed EIS settings), charge to 3.7 V and hold 2 h, then PEIS2 at 3.7 V, then charge to 4.0 V, hold for 2 h, PEIS (EIS1), charge to 4.3 V, hold for 2 h, PEIS1, charge to 4.5 V, hold for 4 h, PEIS1, hold for further 44 h and PEIS1. Then, discharge to 3 V and hold for 4 h. This routine is repeated. Right: End routine. After completing the desired number of repetitions of the hold routine the cell was charged to 3.7 V, held there for 12 h and then left resting until the cell was disassembled (within 48 h).

Ar atmosphere in a 94:3:3 mass ratio of the solid components and 54% of solid mass fraction. The resulting slurry was mixed in a planetary mixer for 20 min and then cast onto aluminum foil which was heated to 60 °C during tape casting. Later, the cathode sheet was dried for 12 h at 120 °C in vacuum and then punched in 12 mm diameter cathodes, pressed at 200 MPa and weighed. The electrode loading was comparably low with ≈4 mg cm^{-2} to avoid lithium concentration gradients within the cathode during operation. This mass loading corresponds to areal capacities of 1.1 mAh cm^{-2} assuming a theoretical specific capacity of 275.1 mAh g^{-1} or to 0.8 mAh cm^{-2} for 200 mAh g^{-1}. The latter specific capacity was used for calculating currents.

For the construction of 3-electrode cells (setup in Figure S20, Supporting Information) all components were assembled within a pouch bag. For the anode, a stainless-steel spacer and a lithium chip (MSE Supplies LLC, Tucson, USA) with a diameter of 14 mm and a thickness of 600 µm were used after mechanically removing the passivation layer from the lithium. Between anode and cathode, two glass fiber separators (GF/D – Whatman, Global Life sciences solutions USA LLC, Marlborough, USA) with each 70 µL of LP40 (1 M $LiPF_6$ in EC:DEC = 50v:50v, MU Ionic Solutions Corporation, Tokyo, Japan) were placed. Between those, an insulated gold wire (50 µm thickness, Goodfellow GmbH, Hamburg, Germany) was introduced as reference electrode. Note that the Au wire was burnt to remove the insulation and washed at the tip, thereby increasing the surface area for lithiation and its longevity. The pouch bag was sealed under 0.002 MPa vacuum.

Electrochemical Procedures: For each 3-electrode cell the gold wire was first lithiated from the anode at a current of 1 µA until the potential dropped to 200 mV versus Li^+/Li, which typically took up to 7 h. The potential was monitored overnight for stability and typically had ≈310 mV versus Li^+/Li.

The cycling procedure for 3-electrode cells is depicted in **Figure 11**. First, two formation cycles at 0.1 C between 3.0 and 4.5 V (with 2 h holds at 4.5 and 3 V) were performed. Then, an impedance measurement (after a hold period) and a 0.1 C charge with an additional hold step were run at the voltages 3.0, 3.7, 4.0, 4.3 and 4.5 V, respectively. Next, the voltage was held at 4.5 V for 44 h (so the total time at 4.5 V amounts to 48 h), an additional EIS at 4.5 V and a subsequent 0.1 C discharge to 3.0 V and a 4 h hold were applied. Consequently, the number of loops of this procedure determine the total runtime and the time at 4.5 V.

Within the experiment, PEIS was performed with two different parameter sets. A quick scan (PEIS1) was run from 200 kHz to 10 mHz with an amplitude of 10 mV using 2 measurements per frequency and Biologics built-in drift correction. The long scan (PEIS2) was applied at 3.7 V and run from 200 kHz to 100 µHz, where in the interval from 3 mHz to 100 µHz only 1 measurement per frequency was made to keep the measurement time of PEIS2 below 12 h.

All cells, harvested for *post mortem* analysis, were subjected to a final charge up to 3.7 V versus Li^+/Li, held at this potential for 12 h and then rested for at least 12 h. This ensures comparable measurement conditions between the cells and avoids, e.g., potential-dependent beam damage during TEM analysis. For the experiments, six identical cells were assembled and subjected to the same protocol with different numbers of loops over the hold routine (highlighted in orange in Figure 11).

Cathode Harvesting: The 3-electrode cells were built in subsequent weeks to allow for electrode harvesting and further chemical analysis via SIMS on the same day. This ensures that there was no effect from the storage time of harvested samples. To harvest a cell (after the final charge and hold at 3.7 V), the pouch bag was opened under Ar atmosphere and the cathode was extracted. It was washed in 1 mL DEC for ≈1 min, rinsed carefully with 2 times 100 µL fresh DEC, and then dried in vacuum for 10 min. However, it was challenging to completely remove all electrolyte residues. This can influence the collected surface data, especially when using SIMS, due to the high sensitivity and ionization probability of PF_6^-. This washing protocol was designed to achieve a practical balance between careful washing and ensuring sample-to-sample reproducibility.

ToF-/Orbitrap-SIMS: The washed cathodes were fixed to a Leica stub using double-sided adhesive tape (Tesa SE, Norderstedt, Germany). A ToF-SIMS M6 hybrid instrument (IONTOF GmbH, Münster, Germany) equipped with a 30 kV Liquid metal ion gun (LMIG) for analysis was used for the ToF-SIMS measurements. Samples were transferred to the instrument under Ar atmosphere using a Leica EM VCT500 shuttle (Leica Mikrosysteme GmbH, Wetzlar, Germany). Measurements were conducted in spectrometry mode in negative polarity using Bi_3^+ as primary ion species. The signal intensity was ≈100 000 counts/s, achieving a mass resolution of FWHM $m/\Delta m \approx 5300$ u at $m/z = 19.00$ u (F^-).

A low-energy flood gun was used for charge compensation. The analysis area was set to 150 × 150 μm^2, with a resolution of 64 × 64 pixels and a cycle time of 85 µs, corresponding to a mass range of m/z = 0–394 u. The primary ion current was $I \approx 0.066$ pA. Surface spectra were acquired under static limit conditions with a dose density limit of 5 × 10^{11} ions cm^{-2}. Calibration was performed using Li^-, F^-, Cl^-, NiO_2^-, C_8^-, and PF_6^- fragments.

For the principal component analysis, a mass interval list comprising 90 manually assigned fragments (given in Section S11, Supporting Information) was utilized to ensure accurate chemical interpretation of the results. SIMS data were normalized to total ion counts, standardized into a data matrix, and then used for PCA.

Depth profiling was conducted using the Orbitrap analyzer of the M6 hybrid SIMS instrument, which mitigates topographical effects during depth profiling. In this mode, the LMIG operated in long-pulse mode with a 15 kV Bi primary beam and a 400 µm aperture. Long-pulse mode does not allow the application of a mass filter to the primary ions. An Orbitrap Q Exactive mass spectrometer (Thermo Fisher Scientific Inc., Waltham, USA) was used for analysis. Measurements were taken over a 450 × 450 μm^2 area, with a mass range of m/z = 50–750 u and a primary ion current of $I \approx 600$ pA. The analysis duration was 900 s, achieving a mass resolution of FWHM $m/\Delta m \approx 407\,866$ at $m/z = 78.9587$ u (PO_3^-). Orbitrap calibration was performed using an internal silver reference.

XPS: The washed cathodes were fixed on the sample holder using double-sided adhesive tape (Tesa SE, Norderstedt, Germany). A PHI VersaProbe IV instrument (ULVAC-PHI, Chigasaki, Japan) was used for XPS measurements. Samples were transferred under Ar atmosphere using a dedicated transport vessel (ULVAC-PHI, Chigasaki, Japan).

Monochromatic Al-K_α radiation (1486.6 eV) served as X-ray source, with a power of 50 W and a beam voltage of 15 kV. The X-ray beam diameter was 200 µm. Detailed spectra for F 1s, Li 1s, C 1s, O 1s, P 2p, Al 2p, Ni 2p, Mn 2p, and Co 2p were acquired with a step size of 0.2 eV and a pass energy of 55 eV. All spectra were calibrated using the adventitious carbon peak at ≈285 eV.

TEM: TEM samples of the electrodes were prepared by dual-beam focused ion beam (FIB, Helios NanoLab 460F1, FEI, Eindhoven, Netherlands) using a 5–30 kV Ga ion beam. A carbon coating of 2 µm was applied as protection layer. After the lift-out, the lamella was thinned to 1 µm thickness by applying 30 kV. Subsequently, the voltage was reduced to 16 kV to minimize beam-damage effects. A final polishing step was performed at 5 kV. All lamellas reached a thickness of less than 100 nm, were stored under vacuum and subjected to Ar plasma cleaning immediately prior to their transfer to the TEM. HAADF-STEM images were obtained with an aberration-corrected TEM (Spectra 300, Thermo Fisher Scientific, Eindhoven, Netherlands) operated at 200 kV and 300 kV, with a current of ≈25 pA and a convergence angle of 25.4 mrad. For the elemental and spectral analysis, EELS was performed at 200 kV, with an energy resolution of 1.3 eV and a convergence angle of 21 mrad.

Supporting Information

Supporting Information is available from the Wiley Online Library or from the author.

Acknowledgements

K.V. and S.S. contributed equally to this work. The authors gratefully acknowledge funding by the BMBF (Federal Ministry for Education and Research, Germany) within AQua-POp (grant no. 03XP0329A, Aqua Cluster of Competence) and FB2-Hybrid (grant no. 03XP0428E, FestBatt Cluster of Competence). J.K.E. acknowledges financial support of the Hessian State Ministry of Higher Education, Research, and the Arts (HMWK) and computational resources provided by the HPC Core Facility and the HRZ of the Justus-Liebig-University Giessen.

Open access funding enabled and organized by Projekt DEAL.

Conflict of Interest

The authors declare no conflict of interest.

Data Availability Statement

The data that support the findings of this study are available from the corresponding author upon reasonable request.

Keywords

cathode electrolyte interphase (CEI), charge transfer resistance, high-voltage, lithium-ion batteries (LIB), nickel-rich NCM

Received: April 16, 2025
Revised: May 23, 2025
Published online:

[1] J. Wen, D. Zhao, C. Zhang, *Renew. Energy* **2020**, *162*, 1629.
[2] L. de Biasi, A. O. Kondrakov, H. Geßwein, T. Brezesinski, P. Hartmann, J. Janek, *J. Phys. Chem. C* **2017**, *121*, 26163.
[3] H.-J. Noh, S. Youn, C. S. Yoon, Y.-K. Sun, *J. Power Sources* **2013**, *233*, 121.
[4] D.-S. Ko, J.-H. Park, B. Y. Yu, D. Ahn, K. Kim, H. N. Han, W. S. Jeon, C. Jung, A. Manthiram, *Adv. Energy Mater.* **2020**, *10*, 2001035.
[5] S. Speidel, T. Bräunl, *Renew. Sustainable Energy Rev.* **2014**, *40*, 97.
[6] L. Hartmann, L. Reuter, L. Wallisch, A. Beiersdorfer, A. Adam, D. Goldbach, T. Teufl, P. Lamp, H. A. Gasteiger, J. Wandt, *J. Electrochem. Soc.* **2024**, *171*, 060506.
[7] Z. W. Lebens-Higgins, S. Sallis, N. V. Faenza, F. Badway, N. Pereira, D. M. Halat, M. Wahila, C. Schlueter, T.-L. Lee, W. Yang, C. P. Grey, G. G. Amatucci, L. F. J. Piper, *Chem. Mater.* **2018**, *30*, 958.
[8] T. Omiya, A. Ikezawa, K. Takahashi, K. Saito, M. Yonemura, T. Saito, T. Kamiyama, H. Arai, *Energy Adv.* **2024**, *3*, 529.
[9] T. Tsujikawa, K. Yabuta, T. Matsushita, M. Arakawa, K. Hayashi, *J. Electrochem. Soc.* **2011**, *158*, A322.
[10] Y.-S. Kang, S. Y. Park, K. Ito, Y. Kubo, Y. Shin, D. Y. Kim, D.-H. Seo, S. Kim, J.-H. Park, S.-G. Doo, M. Koh, J. A. Seo, K. Park, *J. Power Sources* **2021**, *490*, 229542.
[11] R. Jung, M. Metzger, F. Maglia, C. Stinner, H. A. Gasteiger, *J. Electrochem. Soc.* **2017**, *164*, A1361.
[12] S.-K. Jung, H. Gwon, J. Hong, K.-Y. Park, D.-H. Seo, H. Kim, J. Hyun, W. Yang, K. Kang, *Adv. Energy Mater.* **2014**, *4*, 1300787.
[13] H.-H. Ryu, K.-J. Park, C. S. Yoon, Y.-K. Sun, *Chem. Mater.* **2018**, *30*, 1155.
[14] S. Schweidler, L. de Biasi, G. Garcia, A. Mazilkin, P. Hartmann, T. Brezesinski, J. Janek, *ACS Appl. Energy Mater.* **2019**, *2*, 7375.
[15] F. Lin, I. M. Markus, D. Nordlund, T.-C. Weng, M. D. Asta, H. L. Xin, M. M. Doeff, *Nat. Commun.* **2014**, *5*, 3529.
[16] D. Abraham, R. Twesten, M. Balasubramanian, I. Petrov, J. McBreen, K. Amine, *Electrochem. Commun.* **2002**, *4*, 620.
[17] J. Wandt, A. T. Freiberg, A. Ogrodnik, H. A. Gasteiger, *Mater. Today* **2018**, *21*, 825.
[18] B. L. D. Rinkel, J. P. Vivek, N. Garcia-Araez, C. P. Grey, *Energy Environ. Sci.* **2022**, *15*, 3416.
[19] S. Solchenbach, M. Metzger, M. Egawa, H. Beyer, H. A. Gasteiger, *J. Electrochem. Soc.* **2018**, *165*, A3022.
[20] W. M. Dose, W. Li, I. Temprano, C. A. O'Keefe, B. L. Mehdi, M. F. L. de Volder, C. P. Grey, *ACS Energy Lett.* **2022**, *7*, 3524.
[21] S. L. Dreyer, A. Kondrakov, J. Janek, T. Brezesinski, *J. Mater. Res.* **2022**, *37*, 3146.
[22] W. Li, A. Dolocan, P. Oh, H. Celio, S. Park, J. Cho, A. Manthiram, *Nat. Commun.* **2017**, *8*, 14589.
[23] S. P. Kühn, K. Edström, M. Winter, I. Cekic-Laskovic, *Adv Materials Inter* **2022**, *9*, 2102078.
[24] T. Joshi, K. Eom, G. Yushin, T. F. Fuller, *J. Electrochem. Soc.* **2014**, *161*, A1915.
[25] M. Evertz, F. Horsthemke, J. Kasnatscheew, M. Börner, M. Winter, S. Nowak, *J. Power Sources* **2016**, *329*, 364.
[26] J. Kasnatscheew, M. Evertz, B. Streipert, R. Wagner, S. Nowak, I. Cekic Laskovic, M. Winter, *J. Phys. Chem. C* **2017**, *121*, 1521.
[27] K. Ishidzu, Y. Oka, T. Nakamura, *Solid State Ionics* **2016**, *288*, 176.
[28] S. Oswald, H. A. Gasteiger, *J. Electrochem. Soc.* **2023**, *170*, 030506.
[29] F. Friedrich, B. Strehle, A. T. S. Freiberg, K. Kleiner, S. J. Day, C. Erk, M. Piana, H. A. Gasteiger, *J. Electrochem. Soc.* **2019**, *166*, A3760.
[30] S. Sallis, N. Pereira, P. Mukherjee, N. F. Quackenbush, N. Faenza, C. Schlueter, T.-L. Lee, W. L. Yang, F. Cosandey, G. G. Amatucci, L. F. J. Piper, *Appl. Phys. Lett.* **2016**, *108*, 263902.
[31] E. Bautista Quisbert, F. Fauth, A. M. Abakumov, M. Blangero, M. Guignard, C. Delmas, *Small* **2023**, *19*, 2300616.
[32] B. L. D. Rinkel, D. S. Hall, I. Temprano, C. P. Grey, *J. Am. Chem. Soc.* **2020**, *142*, 15058.
[33] H. Luo, B. Zhang, H. Zhang, Q. Zheng, X. Wu, Y. Yan, Z. Li, Y. Tang, W. Hao, G. Liu, Y.-H. Hong, J. Ye, Y. Qiao, S.-G. Sun, *J. Phys. Chem. Lett.* **2023**, *14*, 4565.

[34] W. M. Dose, I. Temprano, J. P. Allen, E. Björklund, C. A. O'Keefe, W. Li, B. L. Mehdi, R. S. Weatherup, M. F. L. de Volder, C. P. Grey, *ACS Appl. Mater. Interfaces* **2022**, *14*, 13206.
[35] K. M. Scheer, M. Tulloch, I. Hamam, J. J. Abraham, M. B. Johnson, M. Metzger, *J. Electrochem. Soc.* **2025**, *172*, 010511.
[36] R. C. McNulty, E. Hampson, L. N. Cutler, C. P. Grey, W. M. Dose, L. R. Johnson, *J. Mater. Chem. A* **2023**, *11*, 18302.
[37] S. Azam, C. P. Aiken, Q. Meisner, H. MacLennan, W. Song, Q. Liu, D.-J. Yoo, S. Aftanas, J. M. Oxner, C. Liao, M. D. L. Garayt, I. Hamam, Z. Zhang, J. R. Dahn, *J. Electrochem. Soc.* **2024**, *171*, 110510.
[38] W. Li, X. Liu, Q. Xie, Y. You, M. Chi, A. Manthiram, *Chem. Mater.* **2020**, *32*, 7796.
[39] E. M. Erickson, W. Li, A. Dolocan, A. Manthiram, *ACS Appl. Mater. Interfaces* **2020**, *12*, 16451.
[40] S. Lee, W. Li, A. Dolocan, H. Celio, H. Park, J. H. Warner, A. Manthiram, *Adv. Energy Mater.* **2021**, *11*, 2100858.
[41] R. Scipioni, D. Isheim, S. A. Barnett, *Appl. Mater. Today* **2020**, *20*, 100748.
[42] J. Li, W. Li, Y. You, A. Manthiram, *Adv. Energy Mater.* **2018**, *8*, 1801957.
[43] Y. Zheng, M. Ouyang, L. Lu, J. Li, *J. Power Sources* **2015**, *278*, 287.
[44] S. J. Wachs, C. Behling, J. Ranninger, J. Möller, K. J. J. Mayrhofer, B. B. Berkes, *ACS Appl. Mater. Interfaces* **2021**, *13*, 33075.
[45] P. Keil, S. F. Schuster, J. Wilhelm, J. Travi, A. Hauser, R. C. Karl, A. Jossen, *J. Electrochem. Soc.* **2016**, *163*, A1872.
[46] Y. Yu, P. Karayaylali, Y. Katayama, L. Giordano, M. Gauthier, F. Maglia, R. Jung, I. Lund, Y. Shao-Horn, *J. Phys. Chem. C* **2018**, *122*, 27368.
[47] H. Li, N. Zhang, J. Li, J. R. Dahn, *J. Electrochem. Soc.* **2018**, *165*, A2985.
[48] A. van der Ven, G. Ceder, *J. Power Sources* **2001**, *97*, 529.
[49] A. Liu, N. Phattharasupakun, M. M. E. Cormier, E. Zsoldos, N. Zhang, E. Lyle, P. Arab, M. Sawangphruk, J. R. Dahn, *J. Electrochem. Soc.* **2021**, *168*, 070503.
[50] J. Landesfeind, D. Pritzl, H. A. Gasteiger, *J. Electrochem. Soc.* **2017**, *164*, A1773.
[51] M. D. Levi, G. Salitra, B. Markovsky, H. Teller, D. Aurbach, U. Heider, L. Heider, *J. Electrochem. Soc.* **1999**, *146*, 1279.
[52] B. Strehle, F. Friedrich, H. A. Gasteiger, *J. Electrochem. Soc.* **2021**, *168*, 050512.
[53] R. Weber, A. J. Louli, K. P. Plucknett, J. R. Dahn, *J. Electrochem. Soc.* **2019**, *166*, A1779.
[54] R. Morasch, H. A. Gasteiger, B. Suthar, *J. Electrochem. Soc.* **2023**, *170*, 080522.
[55] M.-T. F. Rodrigues, K. Kalaga, S. E. Trask, I. A. Shkrob, D. P. Abraham, *J. Electrochem. Soc.* **2018**, *165*, A1697.
[56] R. Ruess, S. Schweidler, H. Hemmelmann, G. Conforto, A. Bielefeld, D. A. Weber, J. Sann, M. T. Elm, J. Janek, *J. Electrochem. Soc.* **2020**, *167*, 100532.
[57] Z. Lun, A. J. Merryweather, A. Mahadevegowda, S. S. Pandurangi, C. Xu, S. Fairclough, V. S. Deshpande, N. A. Fleck, C. Ducati, C. Schnedermann, A. Rao, C. P. Grey, *Energy Environ. Sci.* **2025**, *18*, 4097.
[58] S. Oswald, M. Bock, H. A. Gasteiger, *J. Electrochem. Soc.* **2023**, *170*, 090505.
[59] N. Tsiouvaras, S. Meini, I. Buchberger, H. A. Gasteiger, *J. Electrochem. Soc.* **2013**, *160*, A471.
[60] W. Li, Z. He, Y. Jie, F. Huang, Y. Chen, Y. Wang, W. Zhang, X. Zhu, R. Cao, S. Jiao, *Adv. Funct. Mater.* **2024**, *34*, 2406770.
[61] J.-N. Zhang, Q. Li, Y. Wang, J. Zheng, X. Yu, H. Li, *Energy Storage Mater.* **2018**, *14*, 1.
[62] S. Fang, D. Jackson, M. L. Dreibelbis, T. F. Kuech, R. J. Hamers, *J. Power Sources* **2018**, *373*, 184.
[63] W. Wang, Q. Yang, K. Qian, B. Li, *J. Energy Chem.* **2020**, *47*, 72.
[64] M. Heber, C. Hess, *Surf. Interface Anal.* **2022**, *54*, 847.
[65] H. Wang, Y.-I. Jang, B. Huang, D. R. Sadoway, Y.-M. Chiang, *J. Electrochem. Soc.* **1999**, *146*, 473.
[66] H. Liu, Z. Xie, W. Qu, E. Dy, S. Niketic, S. Brueckner, K. Tsay, E. Fuller, C. Bock, N. Zaker, G. A. Botton, *Small* **2022**, *18*, 2200627.
[67] J. Li, H. Liu, J. Xia, A. R. Cameron, M. Nie, G. A. Botton, J. R. Dahn, *J. Electrochem. Soc.* **2017**, *164*, A655.
[68] C. Liang, L. Jiang, Z. Wei, W. Zhang, Q. Wang, J. Sun, *J. Energy Chem.* **2022**, *65*, 424.
[69] B. Xu, C. R. Fell, M. Chi, Y. S. Meng, *Energy Environ. Sci.* **2011**, *4*, 2223.
[70] W. Li, J. Reimers, J. Dahn, *Solid State Ionics* **1993**, *67*, 123.